Article

High-Capacity Ion Batteries Based on Ti_2C MXene and Borophene First Principles Calculations

Dmitry A. Kolosov [ID] and Olga E. Glukhova *[ID]

Institute of Physics, Saratov State University, 410012 Saratov, Russia
* Correspondence: glukhovaoe@info.sgu.ru; Tel.: +7-84-5251-4562

Abstract: In this paper, we report an ab initio study of a composite material based on Ti_2C and borophene B_{12} as an anode material for magnesium-ion batteries. The adsorption energy of Mg, specific capacitance, electrical conductivity, diffusion barriers, and open-circuit voltage for composite materials are calculated as functions of Mg concentration. It is found that the use of Ti_2C as a substrate for borophene B_{12} is energetically favorable; the binding energy of Ti_2C with borophene is -1.87 eV/atom. The translation vectors of Ti_2C and borophene B_{12} differ by no more than 4% for in the X direction, and no more than 0.5% in the Y direction. The adsorption energy of Mg significantly exceeds the cohesive energy for bulk Mg. The energy barrier for the diffusion of Mg on the surface of borophene B_{12} is ~262 meV. When the composite surface is completely covered with Mg ions, the specific capacity is 662.6 mAh g^{-1} at an average open-circuit voltage of 0.55 V (relative to Mg/Mg+). The effect of reducing the resistance of borophene B_{12} upon its binding to Ti_2C is established. The resulting electrical conductivity of the composite $Ti_{16}C_8B_{40}$ is 3.7×105 S/m, which is three times higher than the electrical conductivity of graphite. Thus, a composite material based on Ti_2C and borophene B_{12} is a promising anode material for magnesium-ion batteries.

Keywords: MXene; Ti_2C; borophene; magnesium-ion; batteries; diffusion; DFT

1. Introduction

The rapid development of technology has greatly increased the human need for reliable rechargeable batteries with high energy density and long service life. Lithium-ion batteries (LIBs) are currently the most common energy-storage systems and are already widely used in portable electronic devices. However, LIBs have many disadvantages related to the cost and safety of their operation [1]. Magnesium can serve as a promising replacement for lithium [2,3]. Divalent magnesium has a higher energy density than monovalent lithium, which implies a higher theoretical capacity at a lower mass, as well as low cost, availability, and safety.

Magnesium-ion batteries (MIBs) were first reported as early as 2000, when Aurbach et al. developed systems of rechargeable Mg batteries based on Mg_x-Mo_3S_4 [4]. In recent years, this direction has experienced a new round of development. Johnson et al. reported promising cathode materials based on α-V_2O_5 and spinel MgM_2O_4 (M = Cr, Co, Fe, Mn, V) [5]. A cathode based on c-Mg_2MnO_4 with a capacity of 160 mA h g^{-1} at an average potential of 2.1 V and an energy density of 335 W h kg^{-1} was fabricated and tested [6]. Other promising candidates for the role of the cathode material in MIBs are various sulfur compounds. In particular, WS_2 nanostructures were synthesized by the hydrothermal method and used as magnesium battery cathodes [7]. A feature of these cathodes is a high capacity of 142.7 mA h g^{-1} at 100 charge/discharge cycles with a high current density of 500 mA/g. Xue et al. reported the application of a CuS nanoflower cathode material based on a conversion reaction mechanism for highly reversible magnesium batteries with improved electrochemical performance [8]. Magnesium batteries with a CuS nanoflower cathode have a high discharge capacity, of ~207 mA h g^{-1} at 100 mA g^{-1}, and a long service life,

of 1000 cycles at 500 mA g^{-1}. The authors of these papers reported the fast kinetics of Mg^{2+}, which makes it possible to charge and discharge the cathode with a high current. An analysis of recent publications on the topic of MIB cathodes shows the relevance and prospects of this topic.

For the successful application of magnesium in MIB, it is necessary to find a suitable anode material for this metal ion. Currently, promising anode materials are two-dimensional (2D) materials due to their unique physical properties and low diffusion barriers [9]. The most interesting materials for use as the anodes of metal-ion batteries (MIBs) are 2D transition metal carbides (Mxenes), which have high electrical conductivity and good stability [10–15]. However, the direct use of MXenes in MIBs is difficult due to the active surfaces of MXenes [16]. The covalent and van der Waals binding of MXenes to various materials and functional groups leads to an increase in the resistance of the material [17–21]. On the other hand, MXenes can be used as a highly conductive substrates for borophene, which is an energy-intensive material. Recent studies have shown that three morphological forms of two-dimensional boron have a metallic type of conductivity during the entire lithiation process, and also have an extremely low diffusion barrier and high energy consumption [22,23]. However, according to experimental data, borophene requires Ag(110), Au(100), Au(111), and other substrates [24]. A graphene monolayer can be used as a substrate for a borophene monolayer. Using ab initio methods, Yu et al. calculated an α-sheet borophene/graphene heterostructure with a theoretical specific capacity of up to 1763.22 mA h g^{-1} and a diffusion barrier of 353 meV, as well as with a high Li adsorption energy of -2.959 eV [25]. An α-sheet borophene/graphene heterostructure was synthesized by the resonance ball milling method for use as a LIB anode [26]. In this heterostructure, graphene serves as a carrier substrate for borophene, and the borophene/graphene heterostructure was able to inherit the excellent properties of borophene. For the first time, the effect of reducing the diffusion of lithium was revealed during the functionalization of borophene with H and OH groups. The maximum anode capacity was 52.3 mA h g^{-1} at a current of 2 A g^{-1}. Due to the low diffusion of lithium in borophene, the charge/discharge current (2 A g^{-1}) is ~37.6 times the battery capacity (~37.6 C). Furthermore, in [27], using ab initio studies, the stability of a monolayer based on B$_2$C$_3$P boron with an ultrahigh theoretical capacity of 3024 mAh/g for lithium, a low diffusion barrier of 0.33 eV, and a metallic type of conductivity was confirmed.

Surface functionalization with -O, -F atoms, and -OH groups can significantly change the properties of MXene [28]. In our work, the functional group of MXene was a 2D monolayer of borophene B$_{12}$, as an anode active material for magnesium-ion batteries. The substrate used was Ti$_2$C, which is the lightest and most electrically conductive in the MXenes family [29]. The choice of these materials as the anode is explained by the close coincidence of the translation vectors of the borophene B$_{12}$ and Ti$_2$C supercells. Thus, our study will be useful for the development of anode materials based on MXenes and borophene for magnesium-ion batteries.

2. Results and Discussion

2.1. Atomistic Models

The atomistic model of the composite supercell consists of two borophene monolayers and one Ti$_2$C layer (Figure 1). At the initial stage, unit cells of Ti$_2$C and borophene B$_{12}$ were used. The atomic structure of these unit cells is shown in the red frame in Figure 1. The translation vectors are Lx = 3.107 Å, Ly = 5.149 Å for the Ti$_2$C unit cell, and Lx = 2.977 Å, Ly = 5.174 Å for the borophene B$_{12}$.
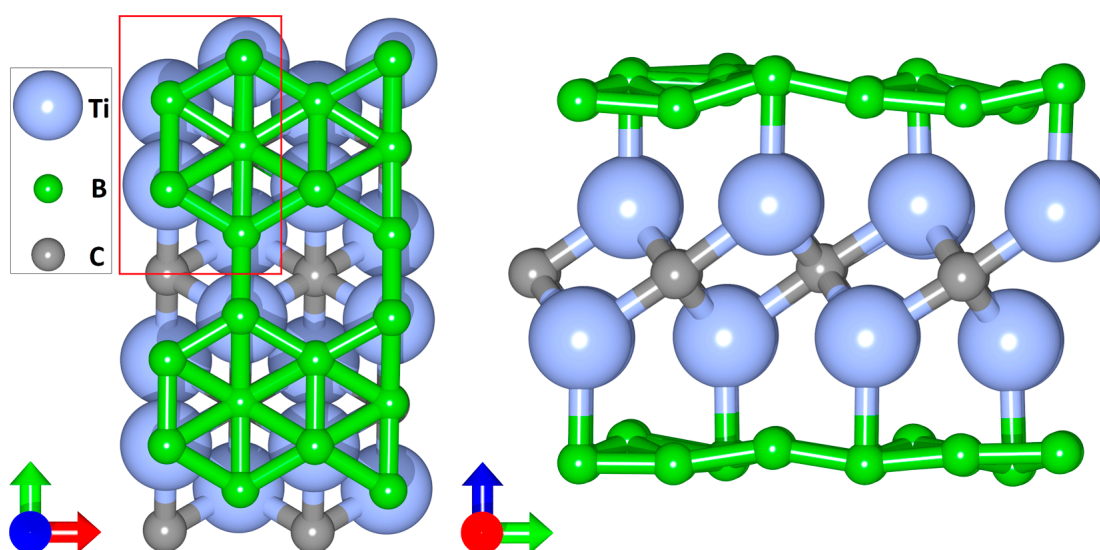
Figure 1. The supercell of a composite structure, $Ti_{16}C_8B_{40}$, in the form of covalently bonded Ti_2C and borophene B_{12}. The left side of the figure shows the view of the structure in the XY plane; the right side is in the YZ plane.

The difference in the translation vector lengths between the Ti_2C and borophene B_{12} unit cells was ~4% along the X axis and ~0.5% along the Y axis, which did not exceed 2.5% on average. The bond length between the Ti and B atoms lay within the range of 2.2 Å~2.3 Å. After the geometric relaxation, the unit cell of $Ti_2C + B_{12}$ had the following translation vectors: Lx = 3.018 Å; Ly = 5.218 Å. Subsequently, the unit cell of $Ti_2C + B_{12}$ was translated along both directions (X and Y axes) and took the final form of the supercell of $Ti_{16}C_8B_{40}$ (see Figure 1) with the translation vectors Lx = 6.04 Å, Ly = 10.43 Å. To assess the energy stability of the composite material $Ti_{16}C_8B_{40}$, the formation energy E_{HoF} was calculated using Equation (1):

$$E_{HoF} = E_{Ti_{16}C_8B_{40}} - \left(E_{Ti_{16}C_8} + E_{B_{40}}\right)/n_{atoms}, \tag{1}$$

where $E_{Ti_{16}C_8B_{40}}$ is the total energy of the composite material, $E_{Ti_{16}C_8} + E_{B_{40}}$ is the total energy of MXene and two borophene B_{12} monolayers, n_{atoms} is the total number of atoms in the structure (64 atoms). The formation energy for this atomistic model is -1.87 eV/atom. As can be seen from the negative value of E_{HoF}, the Mxene+borophene system is energetically favorable and has the right to exist as a result of synthesis. Different placements of borophene during laying should change the properties of the composite. It is also worth considering the appearance of defects on borophene and in maxene (the absence of atoms or oxygen deposition on the surfaces of the films). In our work, we examined in detail one stacking of borophene without defects (Figure 1).

2.2. Electronic and Transport Properties

After checking the energy stability of the composite material, $Ti_{16}C_8B_{40}$, we carried out studies of its electronic and transport properties. Figure 2a shows the DOS for both the composite material and the individual layers of Ti_2C and borophene B_{12}. As can be seen, the composite material $Ti_{16}C_8B_{40}$, as with the composite layers, has a metallic type of conductivity; the metallic properties of the borophene monolayers were enhanced due to the additional electronic states introduced by the Ti_2C.
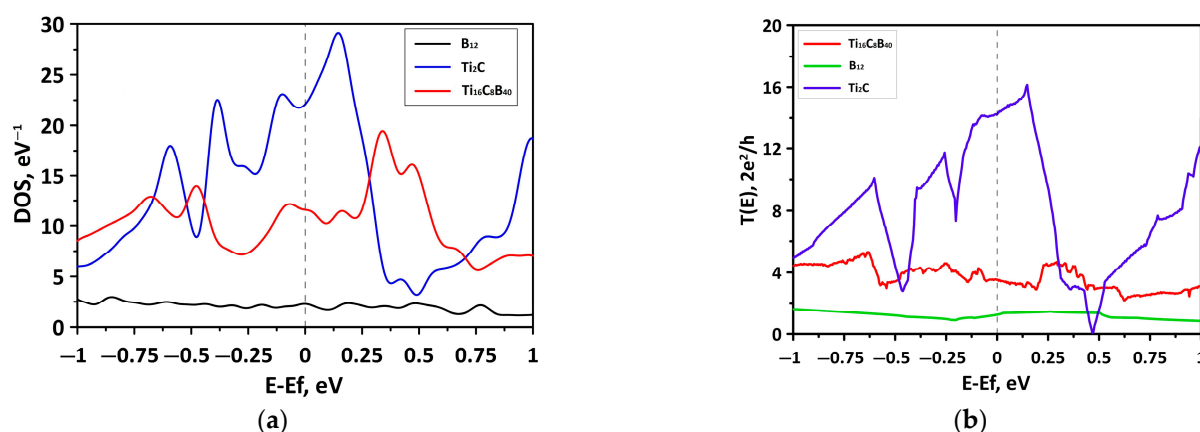
Figure 2. The electronic and energy characteristics of the composite material, $Ti_{16}C_8B_{40}$, and individual layers, Ti_2C and B_{12}: (**a**) DOS; (**b**) electron-transmission function.

Figure 2b shows the curves of the electron-transmission functions T(E) of the composite material and its individual layers. The averaged values of the T(E) function along the zigzag and armchair directions are presented. The behavior of the T(E) curves was qualitatively similar to the behavior of DOS functions. It can be seen that the electrical conductivity of the $Ti_{16}C_8B_{40}$ increased compared to the electrical conductivity of the borophene monolayers. Further, the electrical conductivity of the material $Ti_{16}C_8B_{40}$ was calculated using Equation (2):

$$G = \frac{2e}{h} \int_{-\infty}^{\infty} T(E)F_T(E - E_F)dE \tag{2}$$

where e is the electron charge, h is the Planck constant, E_F is the Fermi energy of the contacts, T(E) is the electron-transmission function, and F_T is the thermal broadening function. The calculated electrical conductivity of $Ti_{16}C_8B_{40}$ is 0.37 S/μm, which is three times higher than that of graphite [30].

2.3. Adsorption, OCV and Diffusion Barrier

To determine the energy-optimal arrangement of the Mg atoms on the surface of the composite material, the adsorption energy was calculated. We considered five variants for the landing of the Mg atoms (Figure 3): two variants with the landing of the Mg atoms inside the hexagon (the landing sites are marked "A" and "E") and three variants with the landing of Mg atoms at the edges of the hexagon (the landing sites are marked "A," "B," and "E"). The most energy-efficient landing sites were "A," "B," and "E". The least favorable in terms of energy were landing sites "C" and "D". In these cases, a titanium atom was located at a close distance under the boron atom. This prevented the curvature of the borophene monolayer. By contrast, in the cases of landing "A" and "E," a carbon atom was located under the boron atom, which was sufficiently distant from both the magnesium atom (point "A") and the boron (point "E"). In the case of landing "B," the boron atom was located under the titanium atom; however, the titanium was much lower than in cases "C" and "D." It should be noted that in all the considered cases of the landing of Mg atoms, a negative value of adsorption energy was observed.
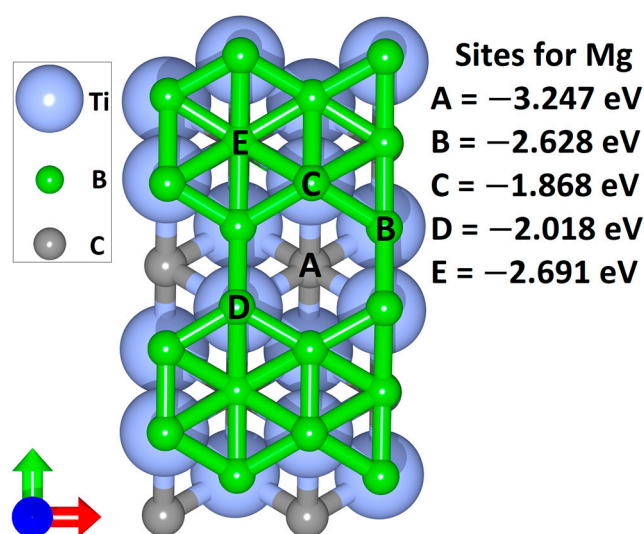
Figure 3. Variants of the arrangement of the Mg atom on the surface of the $Ti_{16}C_8B_{40}$ composite material (the Mg atom is not shown in the figure).

Next, we carried out the placement of Mg atoms on the surface of the composite material at the landing sites "A" and "E" with a further relaxation of the structure geometry (Figure 4a). The Mg atoms were placed both on the top and under the bottom layer of borophene. At the "A" landing sites, the Mg ion was somewhat closer to the borophene monolayer than at the "E" sites due to the location of the boron atom under the Mg ion. It is known that intercalated atoms must donate electrons in the anodes of metal-ion batteries, i.e., acquire a positive charge. In order to reveal this effect, the electronic-charge distribution over the atoms of a supercell was calculated (Figure 4b). As shown in Figure 4b, the magnesium and titanium atoms gave part of the charge to the borophene monolayers, and the carbon atoms acquired a negative charge. This effect was consistent with the value of the electronegativity of atoms according to the dimensionless Oganov scale: carbon atoms are the most electronegative (3.15), followed by boron atoms (3.04) and titanium (2.23) [31]. Magnesium atoms have an electronegativity value of 2.39, which is higher than that of titanium, but due to the presence of a monolayer of borophene, which "shields" titanium, the magnesium acquires a positive charge. In the composite material, $Ti_{16}C_8B_{40}$, borophene acted as a negative charge accumulator. Thus, the composite material $Ti_{16}C_8B_{40}$ is able to oxidize magnesium atoms, which is a key factor in the anode material of metal-ion batteries. In addition, we also calculated the adsorption energy for 16 Mg atoms (complete filling of borophene monolayers) using Equation (3) [32]:

$$E_{ads} = ((E_{Ti_2CB_5} + (nE_{Mg})) - E_{TOTAL})/n \qquad (3)$$

where E_{TOTAL} is the total energy of Mg adsorbed, $E_{Ti_2CB_5}$ is the total energy of pure $Ti_{16}C_8B_{40}$, E_{Mg} is the energy of an isolated Mg atom (an atom in a vacuum), and n is the number of Mg atoms. The calculated adsorption energy for 16 Mg atoms was 2.44 eV/atom (the binding energy has the same value, but with a negative sign), which is higher than the cohesive energy of bulk Mg, which is 1.51 eV/atom [33]. The excess of EADs in the magnesium cohesion energy suggests that at a given concentration, magnesium atoms are not able to form crystalline clusters, which contributes to the safe operation of the anode as part of a magnesium-ion battery. The value of the EADs exceeds the value of the magnesium cohesion energy. Consequently, at this concentration, magnesium atoms are not able to form crystalline clusters, which contributes to the safe operation of the anode as part of a magnesium-ion battery.
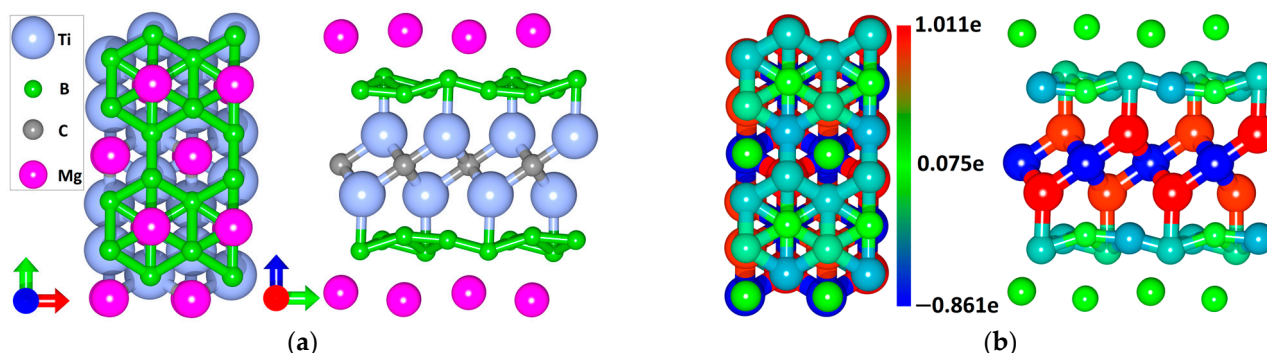
Figure 4. Composite $Ti_{16}C_8B_{40}$ in the presence of Mg atoms: (**a**) supercell; (**b**) Mulliken distribution of electronic charge over atoms.

The next stage of the study was to plot the open-circuit voltage curve. The open-circuit voltage (OCV) profile is one of the most important characteristics for evaluating the performance of the anode material of a metal-ion battery. The open-circuit voltage curve is calculated as the average voltage over parts of the Mg composition domain according to Equation (5). Figure 5 shows the open-circuit voltage profile of an anode material based on $Ti_{16}C_8B_{40}$.
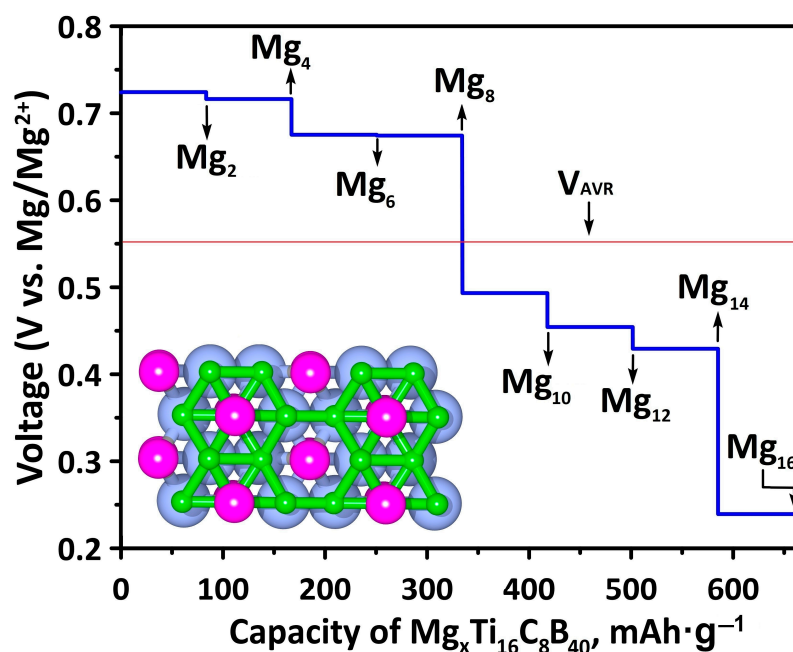

Figure 5. Open-circuit voltage curve of composite material $Mg_XTi_{16}C_8B_{40}$.

As magnesium was placed on the surface of the composite material, $Ti_{16}C_8B_{40}$, the OCV curve decreased from 0.724 V to 0.249 V. When half the capacity ($Mg_8Ti_{16}C_8B_{40}$) was reached, the OCV sharply decreased from 0.674 V to 0.493 V. Similar findings were observed when reaching 100% capacity: the OCV decreased from 0.429 V to 0.249 V. The placement of the Mg atoms occurred simultaneously on both the upper and lower borophene monolayers, one Mg atom each. The maximum capacity of the resulting composite material was 662.6 mAh·g^{-1}, provided that one layer of Mg ions was located on the borophene monolayers. However, according to the data in [34], several layers of Mg ions can be stacked on borophene monolayers, which significantly increases the capacity of the anode material. From the calculated OCV curve, the average voltage $V_{AVR} = 0.552$ V was within the desired potential range for anode materials (0.1 to 1.0 V) [35].

At the final stage of the study, the energy barriers of Mg diffusion along the borophene monolayer were calculated using the NEB algorithm. In total, three cases of diffusion were considered (see Figure 6a–c), in which the Mg ion migrated from one hexagon to the next.
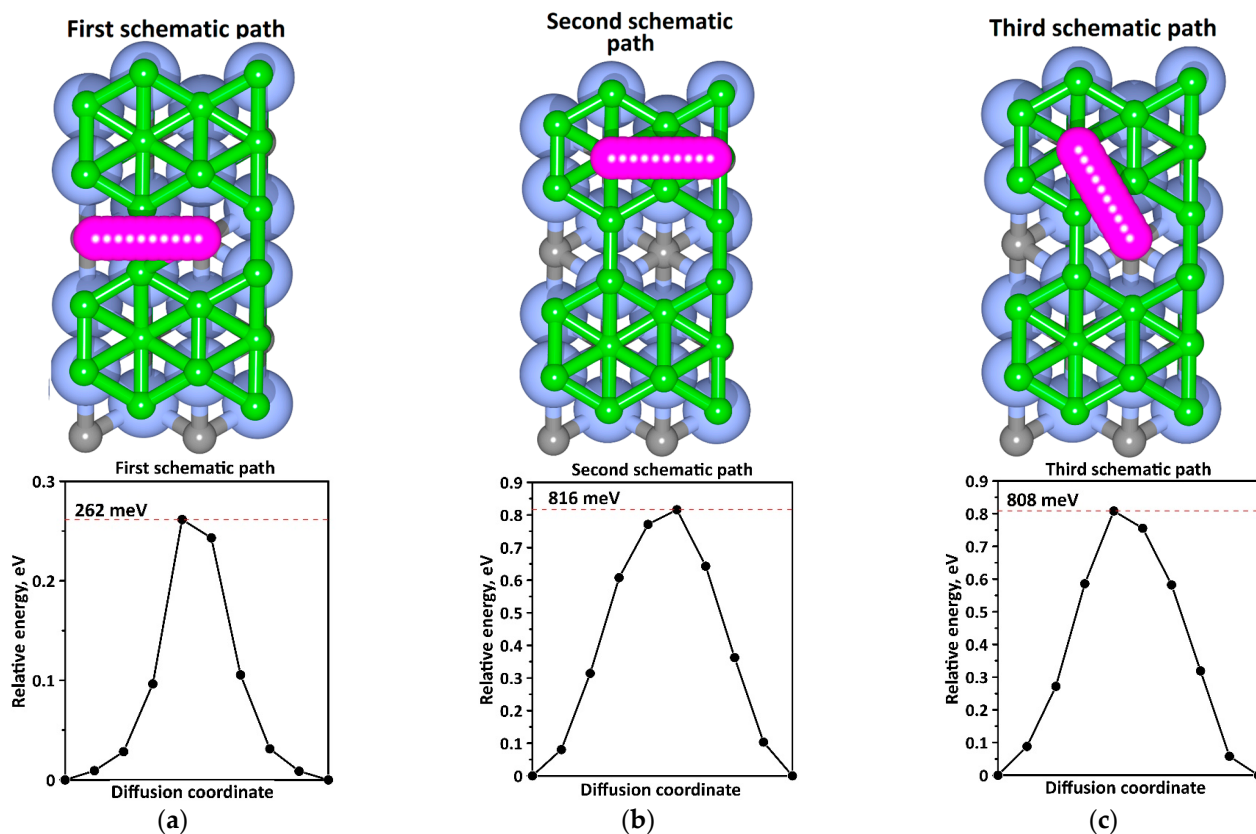

Figure 6. The Mg diffusion paths along the borophene monolayer: (**a**) Mg migration path along empty hexagons; (**b**) Mg migration path along hexagons with a boron atom in the center; (**c**) Mg migration path from the hexagon with the boron atom in the center to the empty hexagon.

In the first case of migration (first schematic path), the Mg ion moved from an empty hexagon to an adjacent empty hexagon. In this case, the maximum diffusion barrier was 262 meV. This was due to the presence of two boron atoms on the migration path. In the second case (second schematic path), the Mg ion migrated from hexagon to hexagon, in the center of which there was a boron atom. The presence of this atom significantly increased the diffusion barrier of the migration to 816 meV, since the Mg ion was located inside the borophene recess (the central boron atom in the hexagon was located deeper than the boron atoms at the vertices of the hexagon). In the third case of ion migration (the third schematic path), the diffusion barrier was slightly lower than in the second case (808 meV), but significantly higher than in the first case. This was caused, firstly, by the presence of a boron atom in the center of the hexagon and, secondly, by the curvature of the borophene monolayer at the point of transition from an empty hexagon to a hexagon with a boron atom in the center. It is worth noting that the diffusion barrier of 262 meV was lower than that of graphite (450~1200 meV) [36], Graphdiyne (350~520 meV) [37] and lithium titanate (300 meV) [38].

The Arrhenius equation was used to estimate the temperature-dependent diffusion transition rate. It follows from this equation that the diffusion constant D was calculated as [39]:

$$D \sim \exp\left(\frac{E_A}{K_B T}\right) \tag{4}$$

where E_A is the activation energy (diffusion barrier) and K_BT is the product of the Boltzmann constant and the temperature. According to Equation (4), the diffusion transition rate for the first case of Mg ion migration was 2.91×10^9 faster than in the second case of migration (second schematic path), and 2.13×10^9 faster than in the third case (third schematic path). Thus, the probability of a diffusion transition from an empty hexagon to another empty hexagon was orders of magnitude higher than in the other cases.

At the next stage of the study, we evaluated the change in the surface area of $Mg_xTi_{16}C_8B_{40}$ during the landing of magnesium on the structure. The starting point (0%) was the clean surface of $Ti_{16}C_8B_{40}$ (without Mg atoms on the surface). Magnesium atoms were placed in pairs: one on the upper side of the structure, the other on the lower side. At each landing, the optimization of the atomic coordinates and translation vectors was carried out. Figure 7a shows the process of changing the surface area of $Ti_{16}C_8B_{40}$ relative to the initial (pure) structure. At the initial stage, the surface area changed by 0.37%. Further, with the addition of two more magnesium atoms, the area decreased to 0.175%. When six magnesium atoms are planted, the area of $Ti_{16}C_8B_{40}$ shrank by –0.2% relative to the area of the initial cell. Further, when planting from 8 to 14 magnesium atoms, the area experienced slight fluctuations from 0.085% to -0.022%. When all the free landing sites were saturated, the surface area decreased to -0.35%. Figure 7a shows that the surface area of $Ti_{16}C_8B_{40}$ changed by no more than 0.37% during the magnesium deposition. Next, to assess the stability of the $Mg_{16}Ti_{16}C_8B_{40}$ structure under the influence of temperature, we performed molecular-dynamics simulations using the canonical (NVT) ensemble in SIESTA. The atomistic structure of the $Mg_{16}Ti_{16}C_8B_{40}$ was exposed to temperatures from 250 K to 450 K for 1.6 ps with a step of 1 fs. The Monkhorst-Pack scheme with $10 \times 6 \times 1$ k-point mesh was used as in the case of geometric relaxation. To maintain the set temperature, a Nose–Hoover thermostat was used; the number of particles and the volume of the atomistic structure did not change during the calculation. The total energy curve is shown in Figure 7b. At the initial step of the MD simulation (300 K), the total energy of the atomistic model was -8722.2427 eV.
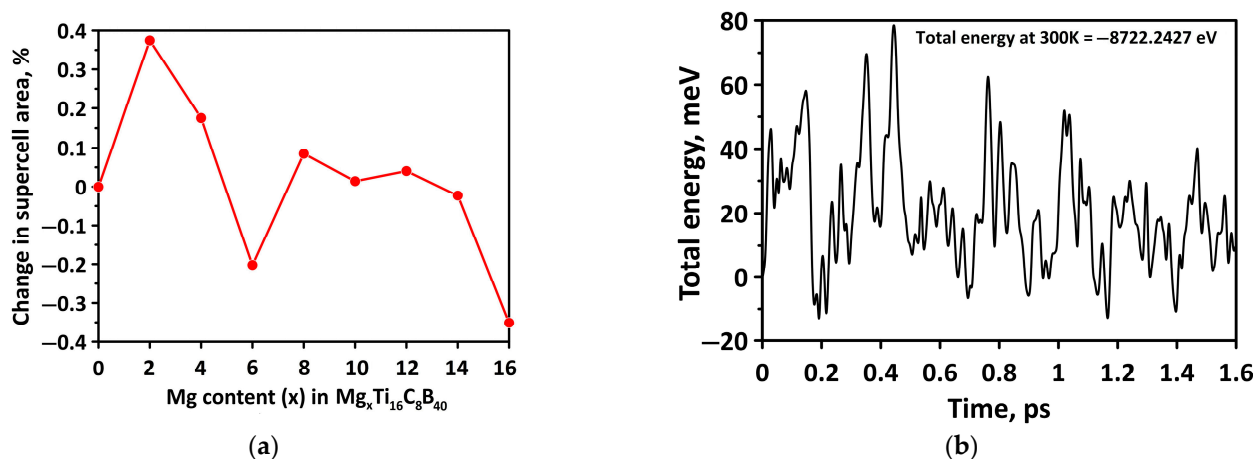

(a)   (b)

Figure 7. Structural-stability study of $Mg_{16}Ti_{16}C_8B_{40}$: (**a**) change in the surface area of $Mg_{16}Ti_{16}C_8B_{40}$ during the process of magnesium embedding; (**b**) change in the total energy of $Mg_{16}Ti_{16}C_8B_{40}$ as a function of time during molecular-dynamics simulation.

During the MD simulation, the temperature varied from 250 K to 450 K. Figure 7b illustrates the good stability of the atomistic structure of the $Mg_{16}Ti_{16}C_8B_{40}$ during heating and cooling. The maximum deviation of the total energy from the initial position was 79 meV, which is ~0.0009% as a percentage. This small deviation in the total energy indicates the excellent structural stability of $Mg_{16}Ti_{16}C_8B_{40}$ due to the formation of covalent bonds of magnesium atoms with boron atoms and of boron atoms with titanium atoms.

3. Materials and Methods

The geometric relaxation of the structures under study was carried out by means of the density functional theory (DFT) using the SIESTA 4.1.5 code [40,41]. The modified Broyden method [42] with Pulay corrections was chosen for the optimization procedure. Optimization was carried out until the forces acting on each atom became equal to 0.025 eV/Å. Double zeta valence plus polarization function (DZP) basis sets were used. We used basis set with generalized gradient approximation (GGA) and Perdew–Burke–Ernzerhof (PBE) parameterization, since these calculation parameters have been clearly proven in terms of both computational accuracy and calculation duration. The van der Waals interaction between the atoms of the structure was taken into account by using the DFT-D2 Grimm corrections. When calculating the geometric parameters of the structures, the Monkhorst-Pack grid was used equal to $10 \times 6 \times 1$. When calculating the density of states (DOS), the Monkhorst-Pack grid was increased to $20 \times 12 \times 1$. The kinetic energy cutoff for wave functions was 350 Ry.

To calculate the electron-transmission function, we used the method of nonequilibrium Green–Keldysh functions (NEGF) implemented in the Siesta package within the TranSiesta module [43]. When performing calculations of quantum transport, the supercell was enlarged by a factor of 3 to create the system of left electrode–scattering region–right electrode. The number of k-points in the direction perpendicular to the current transfer was 100 units. The NEB (nudged elastic band) Siesta algorithm [44] was used to calculate the energy barrier and diffusion paths for magnesium using the LUA scripting language. The NEB algorithm is widely used to find metal diffusion paths in ion batteries [45–47] and is already an integral part of ab initio research on metal-ion batteries. The open-circuit voltage (OCV) in the range $x_1 \leq x \leq x_2$ was found according to Equation (5):

$$V = \frac{-E\left(Mg_{x_2}Ti_{16}C_8B_5\right) - E\left(Mg_{x_1}Ti_2B_5\right) - (x_2 - x_1)E(Mg)}{(x_2 - x_1)q} \tag{5}$$

where $E\left(Mg_{x_2}Ti_{16}C_8B_{40}\right)$ and $E\left(Mg_{x_1}Ti_{16}C_8B_{40}\right)$ are the total energy of $Mg_{x_2}Ti_{16}C_8B_{40}$ and $Mg_{x_1}Ti_{16}C_8B_{40}$, respectively, with x_1 and x_2 intercalated with Mg atoms; E(M) is the energy of the Mg atom in its body-centered cubic (bcc) structure; q is the charge of the Mg ion (q = 2 for Mg).

4. Conclusions

In this work, using the DFT method, an ab initio study of a composite material based on Ti_2C and borophene B_{12} as an anode material for magnesium-ion batteries was carried out. As a result of the study, it was found that: (a) the adsorption energy of Mg exceeds the cohesion energy of Mg (2.44 eV/atom vs. 1.51 eV/atom); (b) the binding energy of Ti_2C with borophene B_{12} is −1.87 eV/atom; (c) the minimum diffusion barrier for Mg ion migration is 262 meV; (d) the specific capacity of the composite at maximum surface coverage with magnesium is 662.6 mAh g^{-1} at an average open-circuit voltage of 0.55 V (relative to Mg/Mg+); (e) the electrical conductivity of the composite material $Ti_{16}C_8B_{40}$ (3.7×105 S/m) is three times higher than that of graphene. An analysis of the change in the surface area of the $Ti_{16}C_8B_{40}$ during the landing magnesium showed an insignificant fluctuation in the surface area, of up to 0.37%. The molecular dynamics calculation revealed the excellent stability of the atomistic structure of $Mg_{16}Ti_{16}C_8B_{40}$ with a maximum deviation in the total energy of ~0.0009% from the initial value. The constructed atomistic model of the composite material has all the qualities of a new-generation anode material for magnesium-ion batteries.

Author Contributions: Conceptualization, O.E.G. and D.A.K.; investigation, D.A.K. and O.E.G.; writing—original draft preparation D.A.K.; writing—review and editing, O.E.G.; visualization, D.A.K.; supervision, O.E.G. All authors have read and agreed to the published version of the manuscript.

Data Availability Statement: Not applicable.

Conflicts of Interest: The authors declare no conflict of interest.

References

1. Wang, Y.-T.; Hao, Y.; Xu, L.-C.; Yang, Z.; Di, M.-Y.; Liu, R.-P.; Li, X.-Y. Insight into the Discharge Products and Mechanism of Room-Temperature Sodium–Sulfur Batteries: A First-Principles Study. *J. Phys. Chem. C* **2019**, *123*, 3988–3995. [CrossRef]
2. Xie, Y.; Dall'Agnese, Y.; Naguib, M.; Gogotsi, Y.; Barsoum, M.W.; Zhuang, H.L.; Kent, P.R. Prediction and characterization of mxene nanosheet anodes for nonlithium-ion batteries. *ACS Nano* **2014**, *8*, 9606–9615. [CrossRef] [PubMed]
3. Zhou, H.; Hu, J. Facile synthesis of multi-walled carbon nanotubes/Co9s8 composites with enhanced performances for sodium-ion battery. *Mater. Lett.* **2017**, *195*, 26–30. [CrossRef]
4. Aurbach, D.; Lu, Z.; Schechter, A.; Gofer, Y.; Gizbar, H.; Turgeman, R.; Cohen, Y.; Moshkovich, M.; Levi, E. Prototype systems for rechargeable magnesium batteries. *Nature* **2000**, *407*, 724–727. [CrossRef]
5. Johnson, I.D.; Ingram, B.J.; Cabana, J. The Quest for Functional Oxide Cathodes for Magnesium Batteries: A Critical Perspective. *ACS Energy Lett.* **2021**, *6*, 1892–1900. [CrossRef]
6. Ruiz, R.; Pérez-Vicente, C.; Rubio, S.; Stoyanova, R.; Zuo, W.; Yang, Y.; Ortiz, G.F. A Cubic Mg_2MnO_4 Cathode for non-aqueous Magnesium Batteries. *Energy Storage Mater.* **2022**, *48*, 12–19. [CrossRef]
7. Guo, W.; Hanaor, D.A.H.; Kober, D.; Wang, J.; Bekheet, M.F.; Gurlo, A. Rechargeable Magnesium Ion Batteries Based on Nanostructured Tungsten Disulfide Cathodes. *Batteries* **2022**, *8*, 116. [CrossRef]
8. Xue, X.; Song, X.; Tao, A.; Yan, W.; Zhang, X.L.; Tie, Z.; Jin, Z. Boosting the cycling stability of rechargeable magnesium batteries by regulating the compatibility between nanostructural metal sulfide cathodes and non-nucleophilic electrolytes. *Nano Res.* **2022**, *16*, 2399–2408. [CrossRef]
9. Xiao, Z.; Li, Z.; Li, P.; Meng, X.; Wang, R. Ultrafine Ti_3C_2 mxene nanodots-interspersed nanosheet for high-energy-density lithium-sulfur batteries. *ACS Nano* **2019**, *3*, 3608–3617. [CrossRef]
10. Naguib, M.; Kurtoglu, M.; Presser, V.; Lu, J.; Niu, J.; Heon, M.; Hultman, L.; Gogotsi, Y.; Barsoum, M.W. Two-Dimensional Nanocrystals Produced by Exfoliation of Ti_3AlC_2. *Adv. Mater.* **2011**, *23*, 4248–4253. [CrossRef]
11. Naguib, M.; Mashtalir, O.; Carle, J.; Presser, V.; Lu, J.; Hultman, L.; Gogotsi, Y.; Barsoum, M.W. Two-Dimensional Transition Metal Carbides. *ACS Nano* **2012**, *6*, 1322–1331. [CrossRef] [PubMed]
12. Yang, E.; Ji, H.; Kim, J.; Kim, H.; Jung, Y. Exploring the possibilities of two-dimensional transition metal carbides as anode materials for sodium batteries. *Phys. Chem. Chem. Phys.* **2015**, *17*, 5000–5005. [CrossRef] [PubMed]
13. Zhao, S.; Kang, W.; Xue, J. Role of Strain and Concentration on the Li Adsorption and Diffusion Properties on Ti_2C Layer. *J. Phys. Chem. C* **2014**, *118*, 14983–14990. [CrossRef]
14. Tang, X.; Guo, X.; Wu, W.; Wang, G. 2D Metal Carbides and Nitrides (MXenes) as High-Performance Electrode Materials for Lithium-Based Batteries. *Adv. Energy Mater.* **2018**, *8*, 1801897. [CrossRef]
15. Simonenko, N.P.; Glukhova, O.E.; Plugin, I.A.; Kolosov, D.A.; Nagornov, I.A.; Simonenko, T.L.; Varezhnikov, A.S.; Simonenko, E.P.; Sysoev, V.V.; Kuznetsov, N.T. The $Ti_{0.2}V_{1.8}C$ MXene Ink-Prepared Chemiresistor: From Theory to Tests with Humidity versus VOCs. *Chemosensors* **2023**, *11*, 7. [CrossRef]
16. Yao, C.; Li, W.; Duan, K.; Zhu, C.; Li, J.; Ren, Q.; Bai, G. Properties of S-Functionalized Nitrogen-Based MXene (Ti_2NS_2) as a Hosting Material for Lithium-Sulfur Batteries. *Nanomaterials* **2021**, *11*, 2478. [CrossRef]
17. Pazniak, H.; Varezhnikov, A.S.; Kolosov, D.A.; Plugin, I.A.; Di Vito, A.; Glukhova, O.E.; Sheverdyaeva, P.M.; Spasova, M.; Kaikov, I.; Kolesnikov, E.A.; et al. Molybdenum Carbide MXenes for Enhanced Selective Detection of Humidity in Air. *Adv. Mater.* **2021**, *33*, 2104878. [CrossRef]
18. Wang, Y.; Zhou, M.; Xu, L.-C.; Zhao, W.; Li, R.; Yang, Z.; Liu, R.; Li, X. Achieving superior high-capacity batteries with the lightest Ti_2C MXene anode by first-principles calculations: Overarching role of S-functionate (Ti_2CS_2) and multivalent cations carrier. *J. Power Sources* **2020**, *451*, 227791. [CrossRef]
19. Hu, J.; Xu, B.; Ouyang, C.; Yang, S.A.; Yao, Y. Investigations on V_2C and V_2CX_2 (X = F, OH) monolayer as a promising anode material for li ion batteries from firstprinciples calculations. *J. Phys. Chem. C* **2014**, *118*, 24274–24281. [CrossRef]
20. Wang, Y.T.; Shen, J.L.; Xu, L.-C.; Yang, Z.; Li, R.; Liu, R.P.; Li, X.Y. Sulfurfunctionalized vanadium carbide mxene (V_2CS_2) as a promising anchoring material for lithium-sulfur batteries. *Phys. Chem. Chem. Phys.* **2019**, *21*, 18559–18568. [CrossRef]
21. Berdiyorov, G.R.; Madjet, M.E.; Mahmoud, K.A. First-Principles Density Functional Theory Calculations of Bilayer Membranes Heterostructures of $Ti_3C_2T_2$ (MXene)/Graphene and AgNPs. *Membranes* **2021**, *11*, 543. [CrossRef] [PubMed]
22. Jiang, H.R.; Lu, Z.; Wu, M.C.; Ciucci, F.; Zhao, T.S. Borophene: A promising anode material offering high specific capacity and high rate capability for lithium-ion batteries. *Nano Energy* **2016**, *23*, 97–104. [CrossRef]
23. Mortazavi, B.; Rahaman, O.; Ahzi, S.; Rabczuk, T. Flat borophene films as anode materials for Mg, Na or Li-ion batteries with ultra high capacities: A first-principles study. *Appl. Mater. Today* **2017**, *8*, 60–67. [CrossRef]
24. Kaneti, Y.V.; Benu, D.P.; Xu, X.; Yuliarto, B.; Yamauchi, Y.; Golberg, D. Borophene: Two-dimensional Boron Monolayer: Synthesis, Properties, and Potential Applications. *Chem. Rev.* **2022**, *122*, 1000–1051. [CrossRef] [PubMed]

25. Yu, J.; Zhou, M.; Yang, M.; Yang, Q.; Zhang, Z.; Zhang, Y. High-Performance Borophene/Graphene Heterostructure Anode of Lithium-Ion Batteries Achieved via Controlled Interlayer Spacing. *ACS Appl. Energy Mater.* **2020**, *3*, 11699–11705. [CrossRef]

26. Yu, J.; Zhou, M.; Yang, M.; Zhang, Y.; Xu, B.; Li, X.; Tao, H. Pristine and Defective 2D Borophene/Graphene Heterostructure as the Potential Anode of Lithium-Ion Batteries. *Adv. Mater. Interfaces* **2022**, *9*, 2102088. [CrossRef]

27. Zhou, D.; Wang, Z.; Cheng, J.; Pu, C. Metallic B_2C_3P Monolayer as Li-Ion Battery Materials: A First-Principles Study. *Processes* **2022**, *10*, 1809. [CrossRef]

28. Cui, W.; Hu, Z.-Y.; Unocic, R.R.; Van Tendeloo, G.; Sang, X. Atomic defects, functional groups and properties in MXenes. *Chin. Chem. Lett.* **2021**, *32*, 339–344. [CrossRef]

29. Kolosov, D.A.; Levitsky, S.G.; Glukhova, O.E. Adhesion and Electron Properties of Quasi-2D Mo_2C, Ti_2C, and V_2C MXene Flakes after Van Der Waals Adsorption of Alcohol Molecules: Influence of Humidity. *Lubricants* **2022**, *10*, 159. [CrossRef]

30. Dihrab., S.S.; Sopian, K.; Zaharim, A. Membrane and bipolar plates materials for regenerative fuel cells. In Proceedings of the 8th WSEAS International Conference on Simulation, Modeling and Optimization (SMO'08), Santander, Spain, 23–25 September 2008; pp. 183–188.

31. Tantardini, C.; Oganov, A.R. Thermochemical electronegativities of the elements. *Nat. Commun.* **2021**, *12*, 2087. [CrossRef]

32. Wu, P.; Li, P.; Huang, M. Potential Application of Graphene/Antimonene Herterostructure as an Anode for Li-Ion Batteries: A First-Principles Study. *Nanomaterials* **2019**, *9*, 1430. [CrossRef] [PubMed]

33. Kittel, C. *Introduction to Solid State Physics*, 8th ed.; John Wiley & Sons, Inc.: Hoboken, NJ, USA, 2005.

34. Rao, D.; Zhang, L.; Meng, Z.; Zhang, X.; Wang, Y.; Qiao, G.; Shen, X.; Xia, H.; Liu, J.; Lu, R. Ultrahigh energy storage and ultrafast ion diffusion in borophene-based anodes for rechargeable metal ion batteries. *J. Mater. Chem. A* **2017**, *5*, 2328–2338. [CrossRef]

35. Guo, G.; Wang, D.; Wei, X.; Zhang, Q.; Liu, H.; Lau, W.; Liu, L. First-Principles Study of Phosphorene and Graphene Heterostructure as Anode Materials for Rechargeable Li Batteries. *J. Phys. Chem. Lett.* **2015**, *6*, 5002–5008. [CrossRef] [PubMed]

36. Thinius, S.; Islam, M.M.; Heitjans, P.; Bredow, T. Theoretical Study of Li Migration in Lithium–Graphite Intercalation Com-pounds with Dispersion-Corrected DFT Methods. *J. Phys. Chem. C* **2014**, *118*, 2273–2280. [CrossRef]

37. Zhang, H.; Xia, Y.; Bu, H.; Wang, X.; Zhang, M.; Luo, Y.; Zhao, M. Graphdiyne: A promising anode material for lithium ion batteries with high capacity and rate capability. *J. Appl. Phys.* **2013**, *113*, 044309. [CrossRef]

38. Zhao, B.; Ran, R.; Liu, M.; Shao, Z. A comprehensive review of Li4Ti5O12-based electrodes for lithium-ion batteries: The latest advancements and future perspectives. *Mater. Sci. Eng. R Rep.* **2015**, *98*, 1–71. [CrossRef]

39. Han, X.; Liu, C.; Sun, J.; Sendek, A.D.; Yang, W. Density functional theory calculations for evaluation of phosphorene as a potential anode material for magnesium batteries. *RSC Adv.* **2018**, *8*, 7196–7204. [CrossRef]

40. Ordejón, P.; Artacho, E.; Soler, J.M. Self-consistent order-N density-functional calculations for very large systems. *Phys. Rev. B* **1996**, *53*, R10441. [CrossRef]

41. Soler, J.M.; Artacho, E.; Gale, J.D.; García, A.; Junquera, J.; Ordejón, P.; Sánchez-Portal, D. The SIESTA method for ab initio order-N materials simulation. *J. Phys. Condens. Matter* **2002**, *14*, 2745–2779. [CrossRef]

42. Johnson, D.D. Modified Broyden's method for accelerating convergence in self-consistent calculations. *Phys. Rev. B* **1988**, *38*, 12807. [CrossRef]

43. Brandbyge, M.; Mozos, J.-L.; Ordejon, P.; Taylor, J.; Stokbro, K. Density-functional method for nonequilibrium electron transport. *Phys. Rev. B* **2002**, *65*, 165401. [CrossRef]

44. Henkelman, G.; Uberuaga, B.P.; Jónsson, H. A climbing image nudged elastic band method for finding saddle points and minimum energy paths. *J. Chem. Phys.* **2000**, *113*, 9901–9904. [CrossRef]

45. Ferrante, F.; Prestianni, A.; Bertini, M.; Duca, D. H_2 Transformations on Graphene Supported Palladium Cluster: DFT-MD Simulations and NEB Calculations. *Catalysts* **2020**, *10*, 1306. [CrossRef]

46. Mortazavi, B.; Dianat, A.; Rahaman, O.; Cuniberti, G.; Rabczuk, T. Borophene as an anode material for Ca, Mg, Na or Li ion storage: A first-principle study. *J. Power Sources* **2016**, *329*, 456–461. [CrossRef]

47. Kavalsky, L.; Mukherjee, S.; Singh, C.V. Phosphorene as a Catalyst for Highly Efficient Nonaqueous Li–Air Batteries. *ACS Appl. Mater. Interfaces* **2019**, *11*, 499–510. [CrossRef] [PubMed]